Sensors and Materials, Vol. 37, No. 7 (2025) 3025–3041
MYU Tokyo

S & M 4100

Reactive Power Optimization Using Improved Salp Swarm Algorithm in Photovoltaic Distribution Network

Shunqing Xu[1] and Hsiung-Cheng Lin[2*]

[1]College of Electrical Engineering, Yancheng Institute of Technology, Yancheng 224051, China
[2]Department of Electronic Engineering, National Chin-Yi University of Technology, Tai-chung 41170, Taiwan

(Received May 7, 2025; accepted July 3, 2025)

Keywords: dynamic reactive power optimization, improved salp swarm algorithm, distributed photovoltaics, distribution network, reactive power compensation device

Distribution network systems usually contain static and dynamic volt-ampere-reactive (VAR) sources such as photovoltaics (PVs) and static VAR compensators (SVCs). It is therefore necessary to optimize the reactive power while considering the flow and voltage constraints in a distribution network. In this study, we aim to minimize the reactive power appearing in the distribution network due to integrated PVs, encompassing devices such as SVCs and capacitors. On the basis of this principle, first, the restriction of switching times of the capacitor bank under the constraint condition is converted into the adjustment cost of the capacitor bank in the objective function. The coupling variables of the capacitor bank can therefore be decoupled. Second, a multi-objective improved Salp Swarm Algorithm (ISSA) for static and dynamic reactive powers is introduced with the involvement of quasi-reverse learning, chaotic mapping, dynamic inertia weight, and a differential mutation operator. The performance fitness function is then established to determine the best solution for minimizing reactive power. The performance results show that the total network loss of static reactive power due to optimization decreases by 23.25% and the maximum network loss decreases by 20.21%. We also verified that the voltage per unit (pu) values meet the criterion of 0.95 pu with a maximum voltage rise of 3.23%. Dynamic reactive power with optimization presents similar network loss and voltage levels, while reducing the number of operations for each capacitor bank by 75%.

1. Introduction

Generally, volt-ampere-reactive (VAR) sources can be produced by generators and equipment such as capacitor banks, static VAR compensators (SVCs), and smart inverters located on a distribution system or at customer facilities.[(1)] Dynamic VAR sources, such as photovoltaics (PVs) power devices and SVCs, show a short response time, whereas static VAR sources, such as mechanically switched capacitors, have a relatively long response time. On the other hand, dynamic VAR devices can continuously control reactive power output instead. In a power system, reactive power usually appears along with a mix of static and dynamic VAR sources.[(2)]

*Corresponding author: e-mail: hclin@ncut.edu.tw
https://doi.org/10.18494/SAM5728

ISSN 0914-4935

Accordingly, constructing large-scale facilities for centralized PV systems is becoming an increasingly challenging problem in power distribution networks.[3,4] For example, dynamic reactive power arises frequently in a distribution network where the PV power supply output continually fluctuates throughout the day.[5,6] To improve the performance of the Salp Swarm Algorithm (SSA), Tawhid and Ibrahim[7] proposed the Chaotic SSA (CSSA) in which SSA was integrated with chaos theory in solving nonlinear systems and unconstrained optimization problems. Fathi *et al.*[8] introduced a differential operator to improve SSA, achieving optimal positions and power factors in PV panels and wind turbines under different scenarios.

In the traditional reactive power optimization, initial solutions are randomly generated and iteratively updated until a predefined maximum number of iterations is reached.[9] Although some methods, such as branch and bound, Newton–Raphson, and linear programming for reactive power optimization, are available, they may be easily trapped in local optimal solutions. Other related methods include capacitor switching, reactive power compensation, and transformer ratio adjustment.[10] Among them, adding reactive power compensation devices and parallel capacitors to optimize the reactive power of the distribution network is currently the most popular method.[11]

Alternatively, artificial intelligence methodologies such as the particle swarm, ant colony, bee colony, and simulated annealing are being used in reactive power optimization.[12–14] In addition to these algorithms, SSA has been extensively utilized across various domains. However, its inherent limitations—weak exploitation, weak convergence, and unstable exploitation and exploration—may affect its efficiency in resolving reactive power optimization problems.

A previous study on high PV penetration addressed voltage imbalance and power loss in distributed grids.[15] It demonstrated that the integration of PV systems proved effective in mitigating transmission line loss. Eid *et al.*[16] introduced an improved marine predator algorithm to minimize the distribution network loss by optimizing the allocation of distributed generation and shunt capacitors. However, the proposed optimization algorithm excessively prioritized loss reduction while overlooking the effect of capacitor switching frequency, potentially causing significant capacitor aging. Gush *et al.*[17] reported the Slime Mold Algorithm to enhance the power flow distribution in power distribution networks. In their study, they did not take into account reactive power compensation devices such as capacitor banks. Therefore, the regulatory capabilities exhibited relative inadequacy in scenarios involving substantial reactive power gaps. Ma *et al.*[18] developed a voltage regulation model for active distribution networks, especially mitigating real-time nodal voltage variations by adjusting the active and reactive powers of each PV plant.

Recent advancements in sensor technologies have made it feasible to acquire real-time operational data, such as voltage and current levels, which are integral for the effective functioning of reactive power compensation systems in distribution networks. In this study, we utilized sensor-based data acquisition to enable real-time monitoring and reactive power optimization in PV distribution networks. On the basis of sensor-collected data, a mathematical model is formulated for reactive power optimization in distribution networks by integrating PVs for real-time control and encompassing both discrete and continuous optimization devices such as SVCs and capacitors.

2. Power Distribution Network with PV

2.1 Impact of distribution network under high proportion of PV access

When a large number of PV systems are connected to the distribution network, their output will affect not only the line flow from the upper-level substation to the load side but also the current distribution, voltage distribution, and network loss of the distribution network. Moreover, the impact of PV systems on the distribution network will change as their capacity and output change. Harmonic pollution can be mitigated by adopting advanced inverter designs with harmonic suppression and filtering functions. This approach can effectively reduce the injection of high-order harmonics into the distribution network, thereby improving power quality and ensuring the stable and reliable operation of the power grid. For this reason, we analyze in this section the impact of grid-tied PV systems on the distribution network in terms of flow distribution, voltage distribution, line current, and network loss.

2.1.1. Power flow distribution

First, let us assume that there are only two main feed lines in the distribution network, where feed line 1 has a total load of $P_1 + jQ_1$ and feed line 2 has a total load of $P_2 + jQ_2$. The PV power source is connected to feed line 2 at node *p*. For clarity, we only analyze the impact of PV grid connection on active power flow in the distribution network, assuming that the power factor of the PV module is 1 and the PV power source only outputs active power with a value of P_{pv}. This means that the reactive power jQ_{pv} is 0. The load at node *p* is depicted as $P_f + jQ_f$, where the total active power load of the nodes before the grid-connected node *p* on feed line 2 is P_{21}, and the total active power load of the nodes after the grid-connected node *p* is P_{22}. Figure 1 shows a double-fed distribution network with PV input.

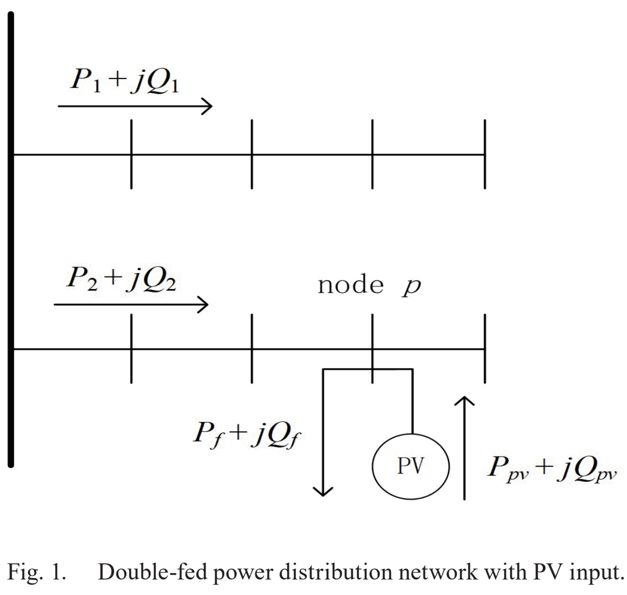

Fig. 1. Double-fed power distribution network with PV input.

By continuously improving the output power of PVs, we can analyze the flow of the double-fed distribution network as follows:

(1) When $P_{pv} < P_f$, the load at node p can fully absorb the input of the PV power source and complete consumption. This means that the load at node p and the active load of line 2 decreas, but the direction of the active power flow in the distribution network remains unchanged.

(2) When $P_{pv} < P_f < P_2$, line 2 can fully absorb the output of the PV power source, but the load at node p cannot fully absorb the input of the PV power source. When $P_{pv} < P_{12}$, the active load of line 2 decreases, but the direction of the overall active power flow in the distribution network remains unchanged. When $P_{pv} > P_{12}$, the bus is still delivering active power to line 2, and at the same time, node p is delivering active power to the end and beginning of line 2. The flow between the bus and node p is reversed, and there is a power-splitting point before the PV integration node p, where the active power is provided jointly by the bus and PVs.

(3) When $P_2 < P_{pv} < P_1 + P_2$, line 2 cannot fully absorb the output of the PV power source, and the unabsorbed portion is absorbed by line 1. The distribution network provides active power to line 1 through the bus, and the PV power source also sends active power to line 1 through line 2. The flow between line 2 and node p is reversed.

(4) When $P_1 + P_2 < P_{pv}$, the active load of both lines cannot fully absorb the output of the PV power source, and the output may be wasted.

2.1.2 Voltage distribution

Figure 2 shows a simplified schematic of a grid-connected node within the power radiation distribution network, which consists of n nodes. Each node i has a load represented by $P_{fi} + jQ_{fi}$, and the impedance of the line connecting node $i - 1$ to node i is $P_i + jQ_i$. Node 0 serves as the balanced node with a constant voltage amplitude, while the voltage amplitude at the i-th node is V_i. The PV power generation system connects to PQ node p, delivering an output power of $P_{pv} + jQ_{pv}$.

(1) Voltage distribution before PV integration into distribution network

Prior to PV integration into the distribution network, voltage is distributed from the bus to the load side of each node. This voltage distribution can be calculated using the voltage drop principle at each node.

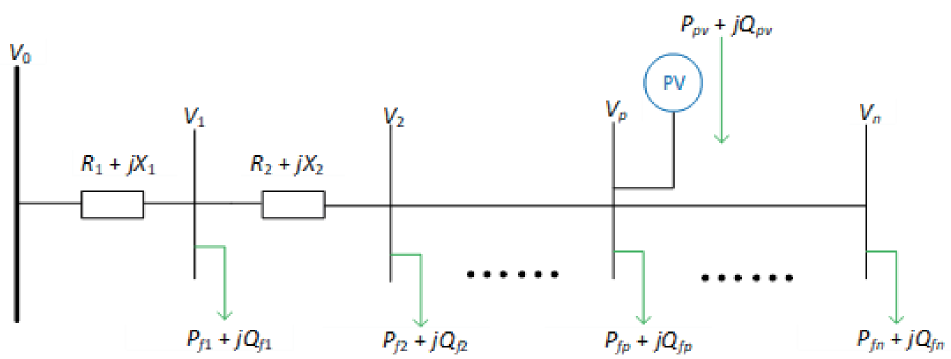

Fig. 2. (Color online) Simplified diagram of interconnected nodes.

$$V_k = V_{k-1} + \Delta V_k + j\delta V_k \tag{1}$$

Here, ΔV_k and δV_k represent the active and reactive components of voltage drop, respectively. Since the reactive component is mainly affected by the voltage phase, the component is mainly affected by the voltage amplitude. If the voltage phase difference between nodes is small relative to the amplitude difference, the effect of reactive power on voltage drop can be ignored.

The voltage difference between nodes is calculated on the basis of the load of each node.

$$\Delta V_k = V_{k-1} - V_k = \frac{R_k \sum_{i=k}^{n} P_{fi} + X_k \sum_{i=k}^{n} Q_{fi}}{V_{k-1}} \tag{2}$$

In a standard distribution network, the loads of nodes consume different amounts of active and reactive powers. When the voltage of the line from the bus to the end of the feed continuously decreases, the voltage of node k can be calculated as

$$V_k = V_0 - \sum_{m=1}^{k} \Delta V_m = V_0 - \sum_{m=1}^{k} \frac{\left(\sum_{i=m}^{n} P_{Li} - P_{pv}\right) R_m + \left(\sum_{i=m}^{n} Q_{Li} - Q_{pv}\right) X_m}{V_{m-1}}. \tag{3}$$

(2) Voltage distribution after PV integration into distribution network

When the distribution network is integrated with PVs, the voltage drop patterns before and after the integration point will change. For ease of analysis, the line is divided into two parts: one is the line between the PV source integration point p and the bus, and the other is the line between the PV source integration point p and the end of the feed line.

For any node k ($0 < k < p$) on the line between the PV source integration point p and the bus, the voltage difference between nodes can be expressed as

$$\Delta V_k = V_{k-1} - V_k = \frac{\left(\sum_{i=k}^{n} P_{fi} - P_{pv,i}\right) R_k}{V_{k-1}}. \tag{4}$$

The given equation indicates that when $P_{fi} < P_{pv}$, $\Delta V_k > 0$, signifying a higher voltage at node k-1 than at node k. Conversely, when $P_{fi} > P_{pv}$, $\Delta V_k < 0$, implying a lower voltage at node k-1 than at node k.

The voltage at node k can be expressed as

$$V_k = V_0 - \sum_{m=1}^{k} \Delta V_m = V_0 - \sum_{m=1}^{k} \frac{\left(\sum_{i=m}^{n} P_{fi} - P_{pv,i}\right) R_m + \left(\sum_{i=m}^{n} Q_{fi} - Q_{pv,i}\right) X_m}{V_{m-1}}. \tag{5}$$

The voltage at the PV integration point p can be obtained as

$$V_p = V_0 - \sum_{m=1}^{k} \frac{\left(\sum_{i=m}^{n} P_{fi} - P_{pv,i}\right) R_m + \left(\sum_{i=m}^{n} Q_{fi} - Q_{pv,i}\right) X_m}{V_{m-1}}. \tag{6}$$

The comparison of Eqs. (4) and (6) shows that if the capacity of the PV source integrated into the grid is small, the voltage on the line between the integration point and the bus will increase after integration. However, as the capacity of the PV source integration increases, the voltage at the PV integration point may exceed the limit, which will damage the safe operation of the distribution network.

2.1.3 Line currents

The current between nodes k-1 and k before the PV grid connection is

$$i_k = \frac{\sqrt{\left(\sum_{m=k}^{n} P_{Lm}\right)^2 + \left(\sum_{m=k}^{n} Q_{Lm}\right)^2}}{V_k}. \tag{7}$$

The current between nodes k-1 and k after the PV grid connection is

$$i_k = \frac{\sqrt{\left(\sum_{m=k}^{n} P_{fm} - P_{pv}\right)^2 + \left(\sum_{m=k}^{n} Q_{fm} - Q_{pv}\right)^2}}{V_k}. \tag{8}$$

As shown by the above formulas, connecting PV to the grid with a small capacity reduces the line current. However, increasing the PV capacity may result in reverse current in the line after PV grid connection, with the current magnitude exceeding that before the PV grid connection.

2.2 Description of static reactive power optimization

The objective function of reactive power optimization is expressed as

$$P_{loss} = \sum_{\substack{i \in N \\ j \in N}} G_j \left(V_i^2 + V_j^2 - 2V_i V_j \cos\theta_j \right), \tag{9}$$

where P_{loss} is the active power loss, N is the total number of network branches, G_{ij} is the conductance on branch i-j, V_i and V_j are the voltages at nodes i and j, respectively, and θ_{ij} is the voltage phase angle difference between nodes i and j.

(1) Equality constraints:

$$\begin{cases} P_{Gi} - P_{Di} = V_i \sum_{j \in N_i} V_j \left(G_{ij} \cos\theta_{ij} + B_{ij} \sin\theta_{ij} \right) \\ Q_{Gi} - Q_{Di} = V_i \sum_{j \in N_i} V_j \left(G_{ij} \cos\theta_{ij} - B_{ij} \sin\theta_{ij} \right) \end{cases} \tag{10}$$

Here, P_{Gi} is the injected active power at node i, P_{Di} is the active power load at node i, V_i is the voltage at node i, θ_{ij} is the voltage phase angle between nodes i and j, G_{ij} is the conductance between nodes i and j, B_{ij} is the susceptance between nodes i and j, N_i is the number of nodes connected to node i, Q_{Gi} is the injected reactive power at node i, and Q_{Di} is the reactive power load at node i.

(2) Inequality constraints:

$$\begin{cases} V_{imin} \le V_i \le V_{imax} \\ Q_{imin} \le Q_i \le Q_{imax} \end{cases} \tag{11}$$

Here, V_{imax} and V_{imin} represent the upper and lower voltage amplitude limits at node i, and Q_{imax} and Q_{imin} represent the upper and lower reactive power compensation capacity limits at node i, respectively.

For grid-tied inverters of PV systems, the maximum compensation capacity Q_{max} is determined by their installed capacity and the active power output at time t, as expressed in

$$Q_{max} = \sqrt{S_{max}^2 - P_t^2}\ , \tag{12}$$

where S_{max} is the installed capacity of the grid-tied inverter of the PV system and P_t is the active power output of the PV system at time t. In this study, we assume that the reactive power output of the PV system is fully compensated for in the case of internal consumption so that it is, therefore, entirely active power.

2.3 Description of dynamic reactive power optimization

In this study, we introduce a dynamic reactive power optimization approach to avoid constraints encountered on the allowable number of capacitor bank actions in the static reactive power optimization. We consider the maximum allowable actions for the reactive power compensation capacitor bank while ensuring that voltage limits are not breached and the total network loss over the 24 periods is minimized. The mathematical model for this optimization is presented as

$$\begin{cases} \min \sum_{t=0}^{23} P_{loss}(B_{Ct}, B_t), \\ s.t. h(B_{Ct}, B_t) = 0, \\ B_{Ct,min} \le B_{Ct} \le B_{Ct,max}, \\ V_{t,min} \le V_t \le V_{t,max}, \\ B_{t,min} \le B_t \le B_{t,max}, \\ \sum_{t=0}^{23} |B_{Ct-1} - B_{Ct}| \le S_C, \end{cases} t = 0,1,2,\ldots,23 \tag{13}$$

where B_{C_t} is the reactive power compensation capacity of each capacitor bank in period t, B_t is the reactive power compensation capacity of each SVC and grid-connected inverter for PV power in period t, V_t is the voltage of each node in period t, $P_{loss}(B_{ct}, B_t)$ represents the total network active power loss in period t, the first constraint $h(B_{ct}, B_t) = 0$ is the flow equation constraint, and S_c is the maximum allowable number of actions of each reactive power compensation capacitor bank within 24 h.

Considering the maximum switching limits of transformers and capacitor banks in the distribution network, the problem of limiting the number of operations in capacitor banks can be converted into the problem of cost adjustment of capacitor banks. To minimize the operational cost of the distribution network,

$$\min f_D = \beta\tau \sum_{t=0}^{23} \Delta P_{loss} + C_A N_C, \tag{14}$$

where f_D is the operating cost of the distribution network, β is the price of electric energy, τ is the optimization time interval, set to 1 h in this study, c_A is the adjustment cost of the reactive compensation capacitor bank, and N_C is the number of operations in the reactive compensation capacitor bank.

The last constraint term in Eq. (19) is no longer necessary. The decoupled dynamic reactive power optimization constraint is given by

$$\begin{cases} s.t.h(B_{Ct}, B_t) = 0 \\ B_{Ct,min} \leq B_{Ct} \leq B_{Ct,max} \\ V_{t,min} \leq V_t \leq V_{t,max} \\ B_{t,min} \leq B_t \leq B_{t,max} \end{cases} \quad t = 0,1,2,...,23\,. \tag{15}$$

This mathematical model eliminates constraints on variable changes, making each period's optimization independent and reducing computational complexity. Additionally, the adjustment cost prevents excessive control device changes solely for network loss reduction.

3. Improved SSA

3.1 Fundamentals of SSA

SSA mimics the foraging behavior of colonial tunicates, featuring two types of search agent in a salp swarm: a leader and some followers.[19] In the entire population's trajectory, i.e., a chain-link group, the leader is heading at the front, influencing only the immediate followers, while the rest move on the basis of the groups ahead. However, its inherent limitations—weak exploitation, weak convergence, and unstable exploration—may affect the efficiency for solving reactive power optimization problems. To address these shortcomings, we improved the standard SSA by introducing adaptive coefficients and dynamic weights in its update mechanisms. This enhancement helps balance convergence speed with population diversity, thereby yielding more robust and accurate optimization results. The specific operational process of SSA is as follows:

(1) Initialize the population

Let the population size be n and the dimension be d. The colonial salp population matrix is initialized as

$$S_d^n = \begin{pmatrix} S_{11} & \cdots & S_{1d} \\ \vdots & \ddots & \vdots \\ S_{n1} & \cdots & S_{nd} \end{pmatrix}. \tag{16}$$

The initialization formula is

$$S = lb + rand(n,b) \times (ub - lb)\,, \tag{17}$$

where ub is the upper limit of the search space, lb is the lower limit of the search space, and $rand(n, d)$ generates a random matrix of n rows and d columns with values ranging from 0 to 1.

(2) Population fitness evaluation and leader selection

Evaluate the initial colonial tunicate population's fitness using the designated fitness function and subsequently arrange them in ascending order on the basis of their fitness scores. The individual with the highest fitness score is designated as the primary food source.

(3) Update the position of the colonial tunicate leader

The leader's position is updated using the following formula:

$$S_d^n(it) = \begin{cases} F_d + c_1(ub_d - lb_d)c_2 + lb_d & c_3 \geq 0.5 \\ F_d - c_1(ub_d - lb_d)c_2 + lb_d & c_3 < 0.5 \end{cases}, \tag{18}$$

where *it* is the current number of iterations, $Sl_d^n(it)$ is the position of the *n*-th salp leader in the *d*-th dimension at the *it*-th iteration, and F_d is the position of the food source in the *d*-th dimension. ub_d and lb_d represent the upper and lower bounds of the search space in the *d*-th dimension, and are random numbers between 0 and 1 that affect the step size and direction of the leader's update, respectively, and dynamically change with the number of iterations according to the following formula:

$$c_1 = 2e^{-\left(\frac{4it}{M\_it}\right)^2}, \tag{19}$$

where *M_it* is the maximum number of iterations for the algorithm. As the number of iterations increases, c_1 gradually decreases, and the step size of the leader's position update also decreases.
(4) Position update for salp followers

The position update rule for salp followers is based on Newton's laws of motion:

$$\begin{cases} Sf_d^n = \dfrac{1}{2}at^2 + vt \\ a = \dfrac{v_{final} - v_0}{t} \\ v_{final} = \dfrac{Sf_d^n - Sf_d^{n-1}}{t} \end{cases}, \tag{20}$$

where t is the time interval, Sf_d^n is the updated position of the *n*-th salp follower in the d-th dimension at the *it*-th iteration, v is the initial velocity, and n is the number of iterations during the algorithm. Since the initial velocity is 0, $S_d^n(it)$ can be expressed as

$$S_d^n(it) = \frac{1}{2}(S_d^n(it) + S_d^{n-1}(it)), \tag{21}$$

where *it* is the current number of iterations and $n \geq 2$.

After updating the position of the salp individuals, boundary handling is performed to ensure that the search space remains unchanged.

3.2 Establishment of improved SSA

3.2.1 Strategy for initial population

There are two key steps involved in the proposed approach. First, a chaotic map, specifically the Tent map described in Eq. (26), is employed to generate half of the population. Following this, the remaining half is generated using the quasi-inverse learning strategy.

Chaotic motion is characterized by its nonlinear, random, regular, and nonrepetitive nature. Owing to the integration of chaotic sequences into the initialization process, this method promotes improved spatial distribution, mitigates local optima traps, accelerates algorithm convergence, and enhances global search capabilities.[20]

$$\begin{cases} 2S^n & 0 \le S^n \le 0.5 \\ 2(1-S^n) & 0.5 \le S^n \le 1 \end{cases} \tag{22}$$

Here, S^n is the n-th individual generated during initialization.

The quasi-inverse learning strategy generates individuals opposing the current population during algorithm initialization, enhancing accuracy and convergence speed without risk of local optima. The formula using this strategy is as follows:

$$S_d^{QOBL} = \begin{cases} \dfrac{lb_d + ub_d}{2} - \left(S_d - \dfrac{lb_d + ub_d}{2} \right) \times rand & S_d < \dfrac{lb_d + ub_d}{2} \\ lb_d + ub_d + S_d - \left(\dfrac{lb_d + ub_d}{2} - S_d \right) \times rand & S_d \ge \dfrac{lb_d + ub_d}{2} \end{cases}, \tag{23}$$

where S_d is the individual salp in the d-th dimension after initialization, S_d^{QOBL} is the quasi-opposite individual of S_d, and ub_d and lb_d are the upper and lower bounds of the search space in the d-th dimension, respectively.

3.2.2 Strategy for individual position updating

In the early SSA iterations, the optimal salp often starts far from the global optimum. To solve this problem, a cumulative effect generated from the swift global exploration can make salps converge towards global optimization as iterations advance.

The improved formula for the leader position updating is as follows:

$$Sl_d^n(it) = Sl_d^n(it-1) + (w \times F_d(it-1) - Sl_d^n(it-1)) \times rand, \tag{24}$$

where it is the current number of iterations, $Sl_d^n(it)$ is the position of the nth leader salp in the d-th dimension in the i-th iteration, and F_d is the position of the food source in the d-th dimension.

Furthermore, the expression for the inertia weight (ω) is

$$\omega = \frac{e^{2(1-it/M\_it)} - e^{-2(1-it/M\_it)}}{e^{2(1-it/M\_it)} + e^{-2(1-it/M\_it)}}, \tag{25}$$

where M_it is the maximum number of iterations of the algorithm. The variation in inertia weight over iterations is illustrated in Fig. 3.

3.2.3 Strategy for population diversity

The differential mutation is used to update the dimension value for the individual. It is expressed as

$$S_d^{n+1} = r_1 \times (F_d - S_d^n) + r_2 \times (S_d^{'} - S_d^n) + S_d^n, \tag{26}$$

where S_d^{n+1} is the position of the nth follower in the d-th dimension at the i-th iteration, F_d is the location of the food source in the d-th dimension, $S_d^{'}$ is the position of a random individual in the d-th dimension of the population, and r_1 and r_2 are random numbers between 0 and 1. Here, the best and worst individuals in the population after each iteration are selected for one-dimensional differential mutation.(21)

4. Performance Results and Analysis

4.1 Static reactive power optimization

The distribution network undergoes daily static reactive power optimization, which is divided into 24 time periods to account for temporal load variations. In this study, we used the IEEE-33

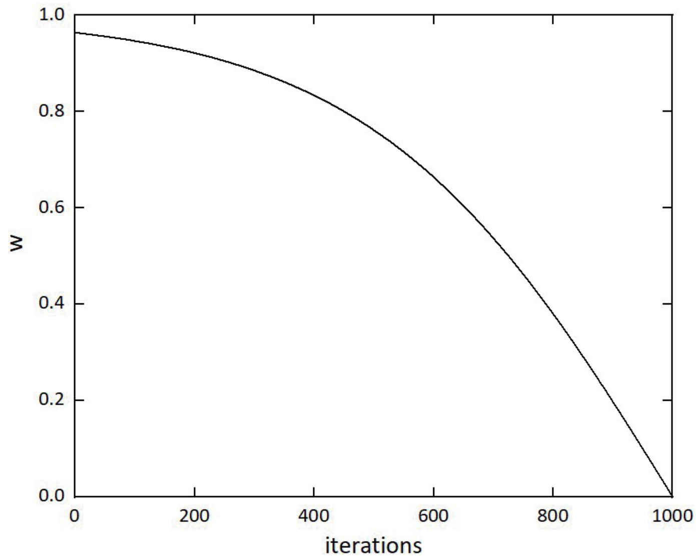

Fig. 3. Variation in inertia weight (ω) over iterations.

node system[22] with two 5 MW PV power sources connected to nodes 16 and 30, where their inverters regulate reactive power. Node 6 features a 1 MVA SVC, whereas nodes 25 and 27 are installed with 20 sets of 50 kVA capacitor banks. The topology diagram of the IEEE-33 node is shown in Fig. 4.

The PV output curve during a typical day in summer is shown in Fig. 5. The curve of distribution network loss with and without improved Salp Swarm Algorithm (ISSA) optimization is shown in Fig. 6. Clearly, the power loss in the network is relatively lower during 10:00–13:00 than during 19:00–21:00, regardless of whether the optimization is carried out. This implies that the integration of PV sources into the distribution network effectively improves the network loss. However, the reactive power compensation using ISSA optimization achieves a better outcome in reducing the network loss at any period.

The statistics of network loss during 24 h are summarized in Table 1, which reveals that the total distribution network loss without optimization is 3.76 MW, with a peak loss of 0.287 MW. On the other hand, ISSA optimization reduces the network loss up to 2.886 MW, down by 23.25%, and the maximum network loss, i.e., 0.229 MW, by 20.21%.

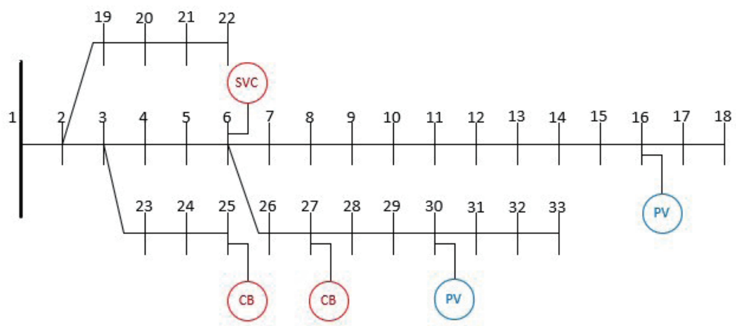

Fig. 4. (Color online) Topology diagram of IEEE-33 node.

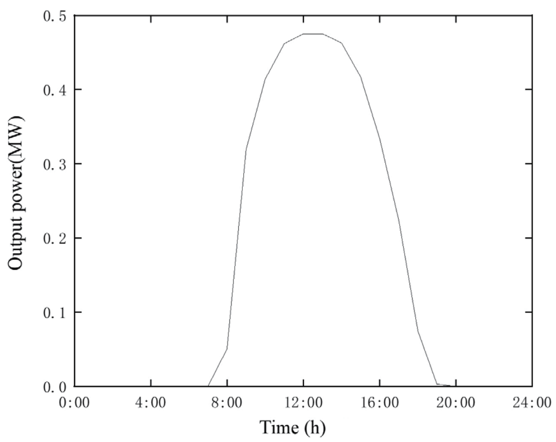

Fig. 5. Typical PV output curve in a day.

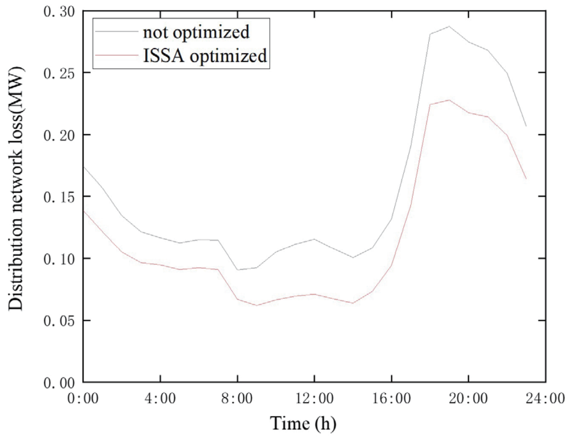

Fig. 6. (Color online) Curve of distribution network loss during 24 periods.

Table 1
Statistics of distribution network loss.

Item	Not optimized	ISSA optimized
Total loss (MW)	3.760	2.886
Maximum loss (MW)	0.287	0.229

After optimization, all node voltages exceed 0.95 pu. Here, a notable increase in voltage standard value occurs at nodes 6–18 and 26–33. However, at nodes 1–3 and 18–24, the optimization process does not have a significant effect on the voltage standard value owing to inherent conditions.

4.2 Dynamic reactive power optimization

In this study, we used the IEEE-33 node system with a maximum of five operations for capacitors. The ISSA optimization algorithm achieves the dynamic reactive power optimization process, as shown in Fig. 7. After the initial optimization, capacitor bank 1 switched 13 times and capacitor bank 2 switched 10 times. To address cost minimization with the number of operations reduced, K-means clustering optimizes switching times.

The PV cell's output power facilitates active power output, enabling power flow calculations and network loss determination for each time interval, as shown in Fig. 8.

Through a comprehensive analysis of the test results, the following conclusions can be obtained:

(1) Within static reactive power optimization, the distribution network's total loss post-optimization constitutes 76.76% of its pre-optimization total loss, with the maximum loss reaching 79.79%. During the peak PV output, the voltage standard experiences a maximum unit value increase of 3.23%.

(2) Within dynamic reactive power optimization, the distribution network's total loss post-optimization is 76.62% of the pre-optimization total loss and the maximum loss reaches

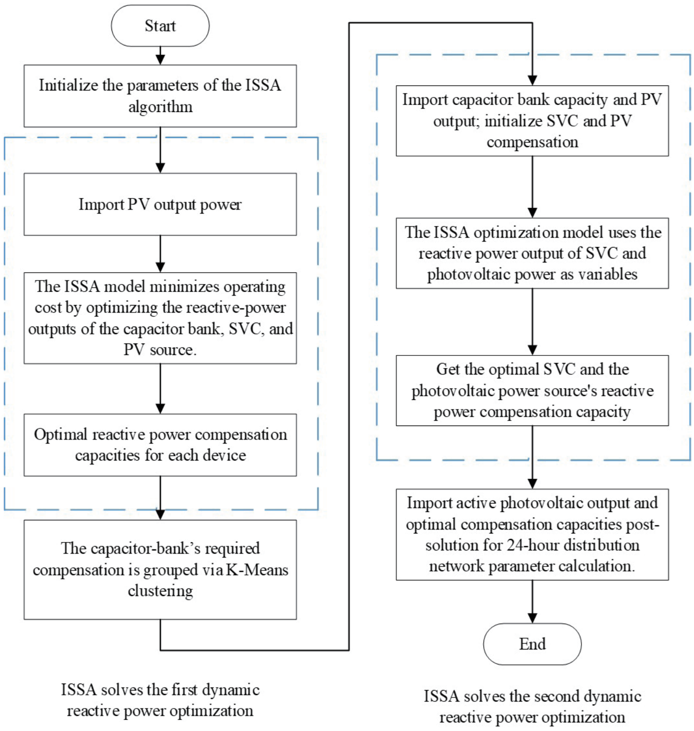

Fig. 7. (Color online) Flowchart of dynamic reactive power optimization.

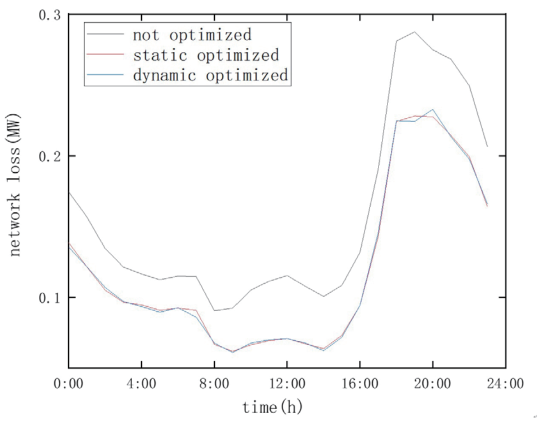

Fig. 8. (Color online) Curves of network loss during 24 periods of time.

81.18%. During the period of maximum PV output, the voltage standard sees a maximum unit value increase of 3.53%. The dynamic optimization of static optimization is superior in terms of network loss and voltage quality, significantly reducing the number of capacitor bank operations by 75% compared with static optimization.

When a large number of PV power sources are connected to the distribution network, their output is random and intermittent, which will affect both the technical and economic indicators of the distribution network. To address this, we propose adding energy storage systems and employing predictive control strategies to smooth power fluctuations, thereby reducing network losses and improving both technical performance and economic benefits. In summary, in this study, we delved into pivotal optimization factors encompassing the reactive compensation capacity of capacitors, grid-connected PV inverters, and SVCs. The optimization procedure meticulously considers operational constraints inherent to capacitor groups. Dynamically, the process integrates the K-means clustering algorithm to ascertain the optimal operation of capacitor groups. The resultant model is a dynamic reactive power optimization framework designed to significantly curtail losses in the distribution network.

5. Conclusions

In this study, we formulated a mathematical model for reactive power optimization in distribution networks with integrated PVs, encompassing both discrete and continuous optimization devices such as SVCs and capacitors. Moreover, the reactive power optimization in PV distribution networks, encompassing both static and dynamic reactive powers, was successfully implemented and evaluated through extensive case studies, demonstrating its practicality and robustness in improving voltage profiles and reducing network losses. ISSA incorporates chaotic mapping, quasi-inverse learning strategies, novel position update strategies, and dimension difference mutation strategies. Compared with other common algorithms, ISSA's various test standards show excellent performance in most test functions. Performance results showed that reactive power optimization leads to enhanced network loss reduction and improved node voltage in the distribution network. With the growing prevalence of controllable resources such as electric vehicles, future studies on reactive power optimization may benefit from exploring its integration with other controllable resources. The islanding effect may compromise the safety and stability of the distribution network when a grid outage occurs, causing distributed generators to continue energizing the grid. For future work, several strategies, such as employing anti-islanding detection methods (active, passive, or communication-assisted), are suggested to enable the timely disconnection of distributed generation. Alternatively, grid-forming controls are added to aid microgrid formation while retaining power to critical loads. Furthermore, adaptive protection schemes can be used to distinguish between normal operations and islanding events, thereby strengthening the robustness and resiliency of the distribution network under the high penetration of PV systems.

References

1 T. Zhang, T. Pu, L. Dong, X. Yuan, Y. Mu, and H. Jia: IEEE Trans. Sustain. Energy **16** (2025) 452. https://doi.org/10.1109/tste.2024.3463177
2 J. Xiao, Y. Zhou, B. She, and Z. Bao: Prot. Control Mod. Power Syst. **10** (2025) 148. https://doi.org/10.23919/pcmp.2023.000210
3 P. K. Singh and D. K. Dheer: Sci. Technol. Energy Transit. **80** (2025) 10. https://doi.org/10.2516/stet/2024108
4 S. Lin, D. Mu, L. Xu, and Z. He: IEEE Trans. Power Deliv. **40** (2025) 365. https://doi.org/10.1109/tpwrd.2024.3495706
5 C. Zhu, S. Yang, and S. Li: J. Renew. Sustain. Energy **17** (2025) 014103. https://doi.org/10.1063/5.0228407

6 J. Liu, C. Niu, Y. Zhang, A. Xie, R. Lu, S. Yu, S. Qiao, and Z. Lin: Appl. Sci.-Basel **15** (2025) 2075. https://doi.org/10.3390/app15042075
7 M. A. Tawhid and A. M. Ibrahim: Math. Comput. Simul. **202** (2022) 113. https://doi.org/10.1016/j.matcom.2022.05.029
8 R. Fathi, B. Tousi, and S. Galvani: Appl. Soft Comput. **132** (2023) 109828. https://doi.org/10.1016/j.asoc.2022.109828
9 C. Wu, W. Li, T. Qian, X. Xie, J. Wang, W. Tang, and X. Gong: J. Energy Storage **76** (2024) 109718. https://doi.org/10.1016/j.est.2023.109718
10 L. Abualigah, M. Shehab, M. Alshinwan, and H. Alabool: Neural Comput. Appl. **32** (2020) 11195. https://doi.org/10.1007/s00521-019-04629-4
11 R. Anilkumar, G. Devriese, and A. K. Srivastava: IEEE Trans. Ind. Appl. **54** (2018) 656. https://doi.org/10.1109/TIA.2017.2740850
12 D. Stanelyte and V. Radziukynas: Energies **13** (2020) 58. https://doi.org/10.3390/en13010058
13 M. Ettappan, V. Vimala, S. Ramesh, and V. T. Kesavan: Microprocess. Microsyst. **76** (2020) 103085. https://doi.org/10.1016/j.micpro.2020.103085
14 A. A. Ogunsina, M. O. Petinrin, O. O. Petinrin, E. N. Offornedo, J. O. Petinrin, and G. O. Asaolu: SN Appl. Sci. **3** (2021) 248. https://doi.org/10.1007/s42452-021-04226-y
15 E. Jamil, S. Hameed, B. Jamil, and Qurratulain: Sustain. Energy Technol. Assess. **35** (2019) 98. https://doi.org/10.1016/j.seta.2019.06.006
16 A. Eid, S. Kamel, and L. Abualigah: Neural Comput. Appl. **33** (2021) 14327. https://doi.org/10.1007/s00521-021-06078-4
17 T. Gush, C.-H. Kim, S. Admasie, J.-S. Kim, and J.-S. Song: IEEE Access **9** (2021) 52164. https://doi.org/10.1109/access.2021.3070155
18 W. Ma, W. Wang, Z. Chen, X. Wu, R. Hu, F. Tang, and W. Zhang: Appl. Energy **284** (2021) 116347. https://doi.org/10.1016/j.apenergy.2020.116347
19 S. Mirjalili, A. H. Gandomi, S. Z. Mirjalili, S. Saremi, H. Faris, and S. M. Mirjalili: Adv. Eng. Softw. **114** (2017) 163. https://doi.org/10.1016/j.advengsoft.2017.07.002
20 Y. Li, M. Han, and Q. Guo: KSCE J. Civ. Eng. **24** (2020) 3703. https://doi.org/10.1007/s12205-020-0504-5
21 X. Zhang, X. Wang, Q. Kang, and J. Cheng: Inf. Sci. **480** (2019) 109. https://doi.org/10.1016/j.ins.2018.12.030
22 M. E. Baran and F. F. Wu: IEEE Trans. Power Deliv. **4** (1989) 1401. https://doi.org/10.1109/61.25627